

Multi-Step Crystallization of Self-Organized Spiral Eutectics

Saman Moniri, Hrishikesh Bale, Tobias Volkenandt, Yeqing Wang, Jianrong Gao, Tianxiang Lu, Kai Sun, Robert O. Ritchie,* and Ashwin J. Shahani*

A method for the solidification of metallic alloys involving spiral self-organization is presented as a new strategy for producing large-area chiral patterns with emergent structural and optical properties, with attention to the underlying mechanism and dynamics. This study reports the discovery of a new growth mode for metastable, two-phase spiral patterns from a liquid metal. Crystallization proceeds via a non-classical, two-step pathway consisting of the initial formation of a polytetrahedral seed crystal, followed by ordering of two solid phases that nucleate heterogeneously on the seed and grow in a strongly coupled fashion. Crystallographic defects within the seed provide a template for spiral self-organization. These observations demonstrate the ubiquity of defect-mediated growth in multi-phase materials and establish a pathway toward bottom-up synthesis of chiral materials with an inter-phase spacing comparable to the wavelength of infrared light. Given that liquids often possess polytetrahedral short-range order, our results are applicable to many systems undergoing multi-step crystallization.

prototypical self-assembly strategy for synthesizing patterned structures across multiple length-scales. The centrality of crystallization phenomena in many scientific fields has spurred decades of research^[1–8] into this “secretive”^[9] process. By tuning the growth conditions, it is possible to steer the system down different kinetic pathways to produce transient or metastable states (e.g., polytetrahedral or disordered phases) on intermediate time-scales.^[10,11] In particular, non-equilibrium routes to metastable states could unveil patterns not seen in equilibrium states. Thus, an understanding of crystallization phenomena is the key to lock into place materials with morphologies and/or functionalities not present in equilibrium states.^[8,10,12,13] Particularly appealing are spiral eutectics,^[14] mixtures of two

1. Introduction

Solidification via crystallization is the seminal procedure controlling the processing of virtually all metals and alloys in use today, yet controlled crystallization can be utilized as a

or more solid phases that grow simultaneously from a parent liquid phase and which arrange into intricate spiraling patterns, in some cases akin to a DNA helix. The intrinsic chirality of spiral eutectics offers a new strategy for rapid, bottom-up manufacturing of large-area photonic materials in the visible/infrared spectrum,^[14,15] owing to the fact that conventional top-down techniques—whose speed and complexity scale up with the number of helices—sets a bottleneck for large-scale production.^[16]

S. Moniri

Department of Chemical Engineering
University of Michigan
Ann Arbor, MI 48109, USA

Dr. H. Bale

Carl Zeiss Microscopy Inc.
Pleasanton, CA 94588, USA

Dr. T. Volkenandt

Carl Zeiss Microscopy GmbH
Oberkochen 73447, Germany

Y. Wang, Prof. J. Gao


Key Laboratory of Electromagnetic Processing of Materials
(Ministry of Education)
Northeastern University
Shenyang 110819, China

Y. Wang, T. Lu, Dr. K. Sun, Prof. A. J. Shahani

Department of Materials Science & Engineering
University of Michigan
Ann Arbor, MI 48109, USA
E-mail: shahani@umich.edu

Prof. R. O. Ritchie

Department of Materials Science and Engineering
University of California
Berkeley, CA 94720, USA
E-mail: roritchie@lbl.gov

 The ORCID identification number(s) for the author(s) of this article can be found under <https://doi.org/10.1002/smll.201906146>.

Despite the technological promise of spiral eutectics, their adoption has been hampered largely by the lack of technical insight into their growth pathway. Thus far, spiral patterns have been observed in the Al-Th,^[17] Al-Ag-Cu,^[18] and Zn-Mg alloy systems,^[19–22] as well as a few non-metallic systems. These reports offer competing proposals for the mechanism of spiral growth, including different growth rates of the eutectic phases,^[19] grain rotations along the eutectic growth direction,^[23] diffusional instabilities caused by a third component,^[24] osmotic flow-driven fingering,^[25] tilted growth in directional solidification,^[26] and thermal fluctuations.^[27] Such phenomena may occur simultaneously or sequentially over the course of crystallization, and thus it is difficult to conclusively isolate the dominant factor for spiral formation. For these reasons, spiral growth is the least understood among all eutectic morphologies (including lamellar and rod^[28]), yet it produces quite dramatic effects. Unraveling spiral growth dynamics requires multiscale 3D and time-resolved measurements.

Here, we pursue a systematic investigation to uncover the origin of spiral growth in Zn-Mg alloys produced via directional solidification (DS). The as-solidified microstructures are chiral, faceted, and periodic with interphase spacing comparable to the

DOI: 10.1002/smll.201906146

wavelength of infrared light. To trace the emergence of such structures from the parent liquid, we employ correlative and multiscale microscopy encompassing fundamentally 3D measurements together with in situ and atomic-resolution imaging. Machine learning (random forest classification^[29]) was used to analyze the 3D datasets for robust tracking of the interfaces of the complex eutectic colonies. We discovered that the metastable MgZn₂ Laves phase nucleates first from the liquid, with crystallographic defects (screw dislocations) that intersect its solid–liquid interfaces and catalyze the spiral growth of the two-phase microstructure. While screws are generally assumed to provide necessary step edges for crystallization,^[30] this work demonstrates that dislocation-driven growth is more widespread than previously imagined; it enables the simultaneous growth of two phases upon spiral eutectic crystallization. These insights open the doors to rapid fabrication and additive manufacturing of 3D chiral photonic materials.

2. Results

2.1. Microstructure Synthesis and Informatics

Synthesis was carried out directionally by the Bridgman–Stockbarger technique, allowing for crystallization at a constant velocity V in a decoupled unidirectional thermal gradient G . In the present investigation of Zn–Mg alloys, the crystallization pathway bifurcates into two competing growth forms, depending on the combination of V and G : thermodynamically stable, rod-like Zn–Mg₂Zn₁₁ and metastable, spiral Zn–MgZn₂ eutectics. We find a transition from the former to the latter at critical velocities, in qualitative agreement with the DS studies by Liu and Jones.^[22] Rigorous analysis of this phase selection, along with microstructural informatics describing the patterns including spirals, are presented in Notes S1–S4, Supporting Information. In what follows, we focus on the emergence of the spiral patterns in Zn–MgZn₂. Out of 195 spirals we examined, we found an equal proportion of spiral handedness (99 right- and 96 left-handed).

2.2. Morphology of Spirals in 3D

Past reports have shown that eutectic spirals mostly develop a helical morphology.^[24,26] To determine if the same holds true for the Zn–MgZn₂ spirals (Figure S1A,2, Supporting Information), we examined the microstructure in 3D via X-ray nano-tomography (nTXM). Machine learning (random forests algorithm^[29]) was utilized to segment the X-ray reconstruction images into the two eutectic phases; Figure S3, Supporting Information, shows excellent agreement between the segmentation output and the eutectic structures visible in the unprocessed data. **Figure 1A** and **Movie S1**, Supporting Information, show the full nTXM region-of-interest displaying multiple spiral eutectic nodules (colonies) and their pyramidal enveloping shapes (false coloring is introduced for better viewing). Outside the colonies is an irregular Zn–MgZn₂ eutectic, characterized by its coarser and non-periodic lamellar spacing. The nTXM reconstruction shows that the spiral colonies are randomly oriented inside the

bulk volume. The internal microstructure is revealed by “cutting” the 3D rendering and displaying it orthogonally along the z -axis, as shown in **Figure 1B**. A close-up view of the same spiral, as shown in **Figure 1C**, provides a wealth of information: i) the outline of the colony is hexagonal (green overlay) throughout, indicating that the crystallographic anisotropy of the MgZn₂ phase plays an important role during solidification; ii) the spirals are characterized by an intra-facet angle $\phi = 10^\circ$ (black lines) and a dihedral angle $2\theta = 18^\circ$; iii) the spiral is terminated at a common nucleation site (**Movie S2**, Supporting Information; shown below to be a polytetrahedral phase); and iv) the spiraling lamellae form continuous, parallel sheets of uniform thickness, unlike the more widespread picture of a DNA helix. In general, for an n -sided cone, the two angles are related as $\phi = 2 \tan^{-1} \left(\sin \theta \tan \left(\frac{180^\circ}{n} \right) \right)$, with which our nTXM results agree. These angular measurements were consistently observed on any randomly chosen spiral colony. Given the complexity of the spiral structure—two phases with nanoscale features—as well as the large volume of data from a typical tomography experiment—millions of voxels—our approach illustrates a case-study of integrating recent developments in data science with experimental techniques, here for microstructure recognition and interface tracking.

The degree of directionality of the colony in the reference (laboratory) frame is quantified by calculating the stereographic projection of the orientations (normals) of solid–solid interfacial patches, as shown in **Figure 1D**. The resulting interface normal distribution (IND) in **Figure 1E** represents the superposition of all lamellar orientations present within the colony and reveals the sixfold symmetry of the Zn–MgZn₂ facet planes, which correspond to the sharp peaks. Overall, the nTXM results provide the first direct evidence for the hexagonal enveloping shape of the spiral Zn–MgZn₂ eutectic colony, terminated at an apex by a nucleation center.

2.3. Epitaxial Relationships between Spiral Constituents in 3D

The complex morphology of the faceted spirals was hypothesized to be influenced by the crystallographic texture (grain rotations^[23]) of the two phases. We utilized 3D-orientation microscopy (electron backscatter diffraction, EBSD) to investigate this possibility and other fundamental properties such as the heteroepitaxial relationship, crystallographic growth direction, and interphase habit plane orientation. **Figure 2A** shows the 3D orientation map of a spiral eutectic colony situated at the junction of three single-crystalline Zn grains (the MgZn₂ lamellae are rendered transparent for clarity). We find a negligible intra-lamellar misorientation ($\approx 1^\circ$) in either phase relative to the full breadth of 3D data. Thus, the spiraling eutectic colony cannot be fully explained by grain rotations. The growth direction of the spiral (the long axis of the hexagonal pyramid, see also **Figure 1D**) is found to be $[0001]_{\text{MgZn}_2}$. In order to visualize the misorientation between the two eutectic phases, we focus on the orientation map of individual 2D cross-sections (**Figure 2B** and **Figure S6**, Supporting Information) along the specimen \hat{z} direction, and superimpose the unit cell on each grain using the respective Euler angles. Both Zn and MgZn₂

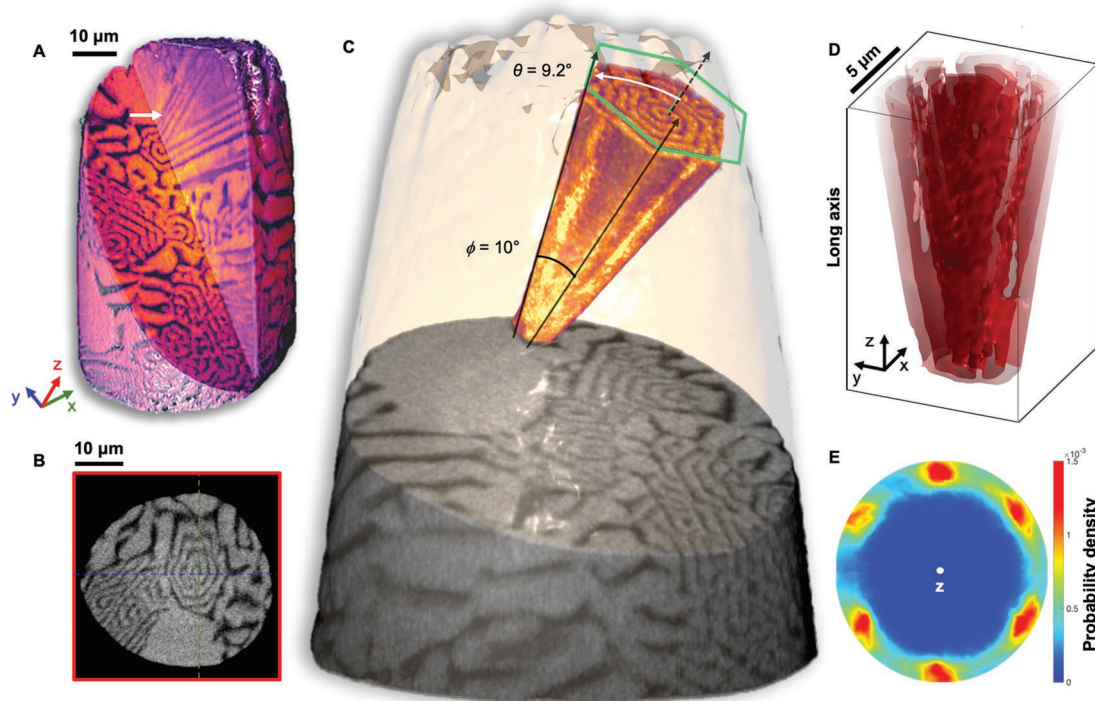


Figure 1. 3D morphology of spiral eutectics. A) Full X-ray nano-tomographic region-of-interest displaying multiple spiral eutectic colonies. The white arrow shows the pyramidal shape of a spiral colony. The reconstruction is cut out to reveal the microstructure internally. The eutectic MgZn_2 and Zn phases are shown in dark and light false colors, respectively. B) View along the cut seen from the y-axis. The eutectic MgZn_2 phase is shown in dark gray. C) Close-up view of the spiral. The spiral colony pointed to by arrow in (A) is extracted, and its surrounding is rendered translucent orange for clarity. The gradation in the spiral's color is due to the false coloring scheme used for visual clarity. The hexagonal enveloping shape along with the inter-planar (dihedral) angle 2θ ($\approx 18^\circ$) and intra-facet angle (10°) are annotated. D, E) Solid–solid interfaces and their directionality within the spiral. The Zn– MgZn_2 interfaces (D) are extracted from the 3D reconstruction and are used to quantify the preferential directionality of the colony in the laboratory frame E). The interface normal distribution (defined in main text) reveals the sixfold symmetry of the solid–solid interfaces, which correspond to the sharp peaks. The sample was grown with $G = 2 \frac{\text{cm}}{\text{cm}}$ and $V = 3.3 \frac{\text{mm}}{\text{s}}$ (Figure S2, Supporting Information).

are single-crystalline within the given colony. The inset in Figure 2B shows the misorientation between the two phases, 75° about $(\bar{2}3\bar{1}2)_{\text{Zn}}$. The two eutectic constituents maintain this epitaxial relationship, including the tilt of the solid–solid interface, across the sample volume (Figures S6 and S7 and Table S2, Supporting Information). The epitaxial assignments are verified by the small ($<3^\circ$) angular deviation between the pairs of coincident planes between Zn and MgZn_2 .

The 3D data also enabled us to obtain the orientation of the solid–solid interfaces by constructing a crystallographic interface normal distribution (CIND), an IND in the crystallographic frame. Specifically, the CIND is found by rotating the interface normals to the crystallographic frame of the MgZn_2 phase using the respective Euler angles. The CIND along $\langle 0001 \rangle_{\text{MgZn}_2}$ (Figure 2C) provides a quantitative intuition into the crystallographic properties of the spiral eutectic. The six peaks in the CIND reveal that the solid–solid interfaces have the $\{70\bar{7}2\}_{\text{MgZn}_2}$ orientation. Interphase boundaries represented on opposite ends of the CIND meet at the apex of the pyramidal spiral, for instance $(\bar{7}072)_{\text{MgZn}_2}$ and $(70\bar{7}2)_{\text{MgZn}_2}$. The interplanar angle is calculated to be $\approx 18^\circ$, corroborating the nTXM observations (cf. Figure 1). Separately, Dippenaar et al. used standard crystallographic formulae to arrive at the indices of the solid–solid interfaces,^[21] also finding that $\{70\bar{7}2\}_{\text{MgZn}_2}$ are the lowest-index

planes. However, they refuted that computation, citing that “it is more likely that ... lower-index [compact] planes in the correct measure yield the average orientation” computed. This would imply the presence of an orientation gradient across the volume of the sample, which in turn could be manifested as a change in the relative tilt of the eutectic phases. Neither of these assertions are supported by our direct 3D EBSD results (Figures S6 and S7 and Table S2, Supporting Information).

2.4. Two-Step Crystallization Pathway

Through in situ synchrotron high-energy X-ray diffraction (HEXRD) under non-equilibrium conditions that favor spiral growth, we tracked the phase formation sequence by acquiring Laue patterns as a function of diffraction angle 2θ . Synchrotron radiation is ideally suited for the detection of low-volume-fraction phases, such as the spiral nucleant. The 400 diffraction spectra collected during 200 seconds of solidification permitted resolving the fast kinetics of nucleation temporally, and the summarized results are shown in Figure 3. The diffraction peak belonging to the first solid phase to form corresponds to MgZn_2 (dashed line at ≈ 1.0 s, $2\theta \approx 2.9^\circ$); meanwhile, peaks belonging to the Zn phase appear ≈ 2 s later. These results show

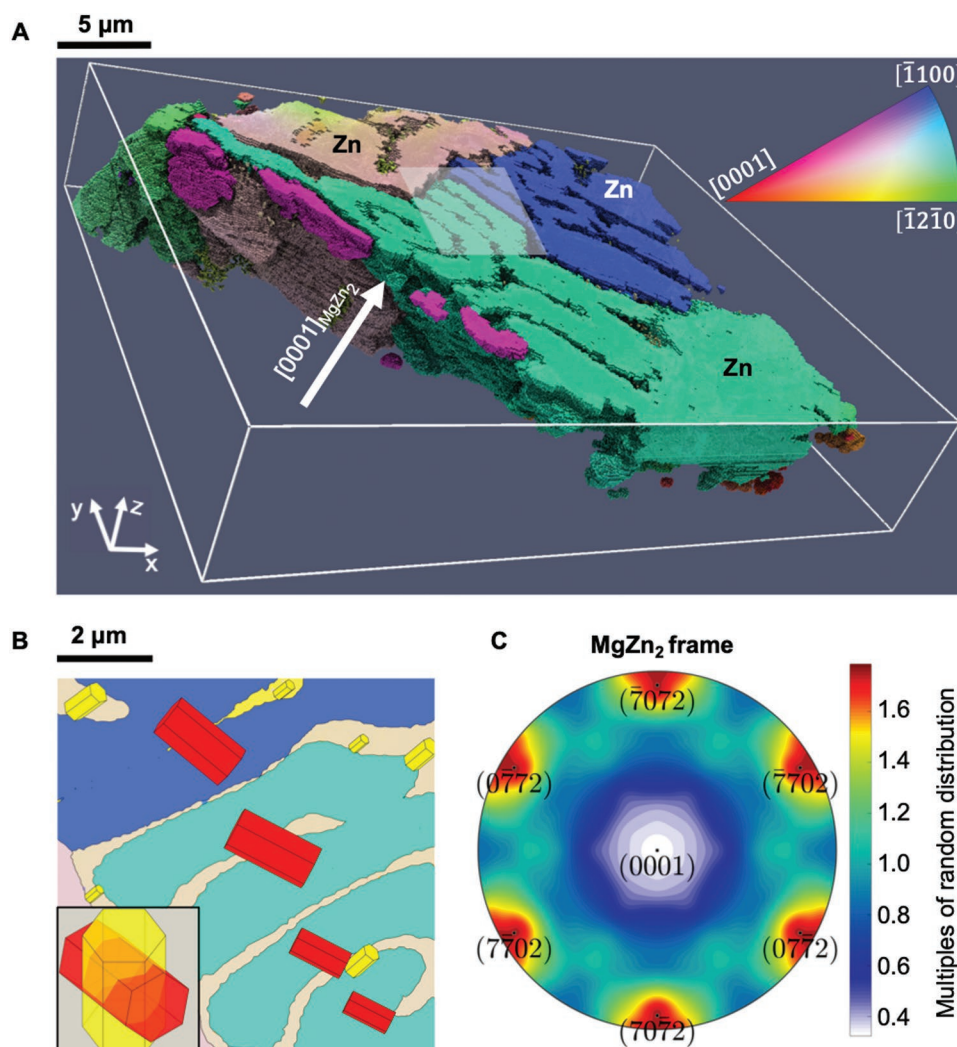


Figure 2. Heteroepitaxial relationship between the two spiral eutectic constituents. A) 3D orientation map (3D EBSD) of a spiral eutectic colony. The spiral is situated at the junction of three single crystalline Zn grains (navy, turquoise, tan). The faceted MgZn_2 phase is rendered transparent for clarity; the Zn grains (voxels) are colored according to their orientation following the stereographic triangle on the top-right. The growth direction of the spiral is along $[0001]_{\text{MgZn}_2}$. B) Orientation map of one representative slice with unit cells superimposed using the respective Euler angles (Zn: red; MgZn_2 : yellow). Facets of the unit cells correspond to the $\{10\bar{1}0\}$ and $\{0001\}$ planes. Both phases are single-crystalline. The map corresponds to the transparent box shown in (A). Inset: the misorientation between the two phases. C) Distribution of the crystallographic orientation of the solid–solid Zn– MgZn_2 interfaces. The plot of crystallographic interface normal distribution (defined in main text) is shown along (0001) axis of MgZn_2 . The six crystallographically symmetric poles of high probability reveal that the solid–solid interfaces have the $\{70\bar{7}2\}_{\text{MgZn}_2}$ orientation. The interplanar angle, for example, between $\{70\bar{7}2\}_{\text{MgZn}_2}$ and $\{70\bar{7}2\}_{\text{MgZn}_2}$ is $\approx 18^\circ$, matching the observation from X-ray nano-tomography (Figure 1). The sample was grown with $G = 2 \frac{\text{°C}}{\text{cm}}$ and $V = 3.3 \frac{\text{mm}^3}{\text{s}}$ (Figure S2, Supporting Information).

the sequence of phase formation and, importantly, provide direct evidence of the initial formation of MgZn_2 particles that serve as nucleants for the Zn– MgZn_2 eutectic. This observation complements the detection of seed crystals in nTXM at the apex of the pyramidal spirals (cf. Figure 1 and Movie S2, Supporting Information).

2.5. Atomic Visualization of Spiral Nucleant

The seed MgZn_2 particles are characterized by a hexagonal outer shape with an open core (white arrows in Figure S2, Supporting Information). They have a coherent lattice with the

MgZn_2 phase of the spiral eutectics but contain more crystallographic defects, as suggested by the hollow core. Using diffraction-contrast transmission electron microscopy (TEM) under the strong two-beam conditions,^[31] as well as atomic-resolution scanning TEM (S/TEM) imaging, we confirm the presence of defects (screw dislocations) within seed MgZn_2 crystals. In the TEM images taken along the $[\bar{1}2\bar{1}0]_{\text{MgZn}_2}$ zone axis shown in Figure 4A,B, dislocation contrast is invisible upon exciting the $(10\bar{1}0)$ family of diffraction spots (Figure 4A). Dislocation lines become visible upon exciting a family of diffraction vectors containing a parallel component to the spiral growth axis, for example, (1011) spot (Figure 4B). Thus, the dislocation lies along the $[0001]_{\text{MgZn}_2}$ direction, which is also the spiral growth

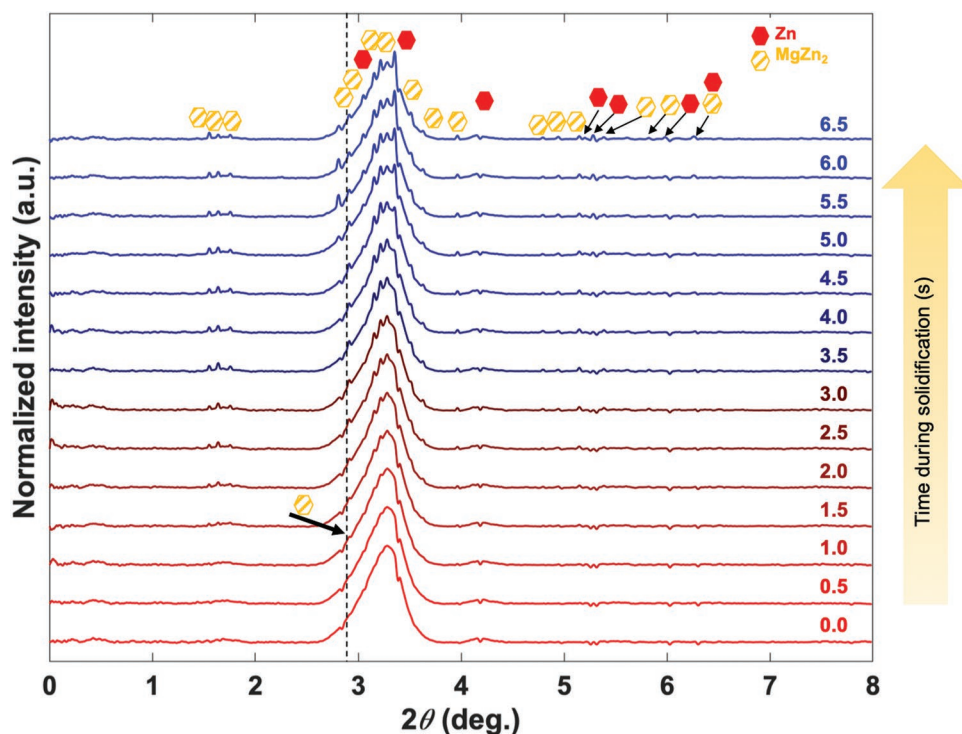


Figure 3. Sequence of phase formation during solidification. The in situ high-energy X-ray diffraction (HEXRD) spectra acquired at the indicated time-steps after the start of solidification (0.0 s) show that MgZn_2 is the first solid phase that forms (dashed line at 1.0 s, $2\theta \approx 2.9^\circ$).

direction (Figure 2A). Since both growth and dislocation directions are along $[0001]_{\text{MgZn}_2}$, this behavior is consistent with a dislocation of screw character. It is important to mention that the “invisibility criterion” invoked above holds for elastically isotropic materials, of which MgZn_2 is not.^[32] Nevertheless, MgZn_2 has a hexagonal crystal structure, so the basal plane and all planes perpendicular to it are elastically symmetric. Consequently, all dislocations that lie on the basal plane or perpendicular to it exhibit pseudo-elastic isotropy, and hence the invisibility criterion is valid for dislocations which lie on such planes.^[31]

The atomic-resolution STEM image in Figure 4C provides a direct visualization of the screw dislocation. The STEM image shows shearing of the planes, characteristic of the side-view of a $c[0001]$ -oriented screw dislocation in MgZn_2 (beam direction: $[11\bar{2}0]_{\text{MgZn}_2}$); colored lines are superimposed to guide the eye. The atomic displacements extend preferentially along the $[0001]_{\text{MgZn}_2}$ direction (Figure S8, Supporting Information). We note that the equal probability of spiral handedness (Note S2, Supporting Information) implies an equal probability of the dislocation sense and, more importantly, is additional evidence of screw-mediated spiral growth.

2.6. Development of Spiral Patterns from Nano- to Micro-Scale

Based on the results above, we propose the following mechanism, shown schematically in Figure 5, for the crystallization of spiral Zn- MgZn_2 eutectics under non-equilibrium conditions (cf. Figure S2, Supporting Information). Under such conditions, MgZn_2 is the first phase to crystallize. The preferential

nucleation of the Laves phase demonstrates that its solid–liquid interfacial energy (and hence, barrier to nucleation) is considerably less than that of the stable $\text{Mg}_2\text{Zn}_{11}$ phase, assuming similar wetting angles.^[33] Spaepen,^[34] Holland-Moritz,^[35] and others^[36] have reasoned that the low interfacial energy is due to the polytetrahedral structural similarity between the melt and the MgZn_2 Laves phase.

The axial screw dislocation of the seed MgZn_2 establishes a spiral ramp that provides self-perpetuating steps which enable spiral growth (Figure 5A). Given the large Burgers vector (≈ 4 nm; Note S5, Supporting Information), as the seed crystal grows, the high strain field around the screw leads to the formation of hollow structures (open cores) in order to relieve the strain energy.^[30] According to Frank’s seminal theory,^[30] it is energetically more favorable to remove the crystalline material adjacent to the dislocation line and create an additional inner surface in the form of a hollow core, compared to retaining the strain energy of the dislocation. This is shown schematically in Figure 5B. We rationalize this observation through an energy balance (Note S5, Supporting Information) between the dislocation strain energy and the energy required for creating the hollow core. A similar phenomenon is reported in other dislocation-prone materials.^[37,38] Here, the open-core dislocation of MgZn_2 is subsequently filled with the other eutectic phase (Zn), forming the micropipes (white arrow in Figure S2, Supporting Information). As revealed by the fixed positions of HEXRD peaks in Figure 3, the strain field survives through the thermal contraction of the bulk volume upon solidification. Thus, our S/TEM results at room temperature are generalizable. Furthermore, we find only an insignificant contribution (Note S5, Supporting Information) to strain relaxation from

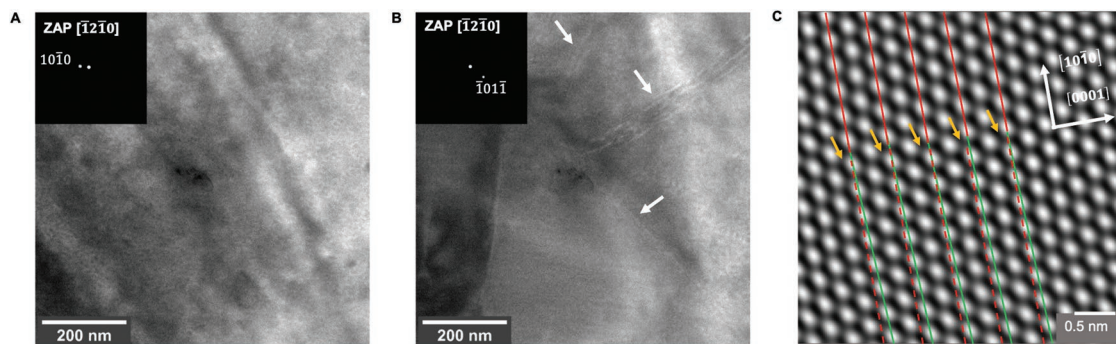


Figure 4. S/TEM observation of screw dislocations within “seed” MgZn_2 crystal. A, B) Diffraction-contrast TEM images taken under the strong two-beam conditions defined by the diffractions as insets to the images near the $[\bar{1}2\bar{1}0]_{\text{MgZn}_2}$ zone axis. Dislocations are invisible upon excitation of diffraction vectors perpendicular to the $[0001]_{\text{MgZn}_2}$ direction, for example the $(10\bar{1}0)$ spot in (A). Dislocation lines become visible (white arrows) when the diffraction vector has a parallel component to the $[0001]_{\text{MgZn}_2}$ direction, for example, the $(\bar{1}01\bar{1})$ spot in (B). Therefore, the dislocation lies along the $[0001]_{\text{MgZn}_2}$ direction, which is also the growth direction (Figure 2). Since both the growth and dislocation directions are along $[0001]_{\text{MgZn}_2}$, this behavior is consistent with a dislocation of screw character. C) Atomic-resolution high-angle annular dark-field (HAADF) image taken along $[\bar{1}1\bar{2}0]_{\text{MgZn}_2}$, showing screw dislocations aligned along $[0001]_{\text{MgZn}_2}$. Solid red and green lines indicate the shearing of atomic planes, characteristic of the side-view of a screw dislocation; dashed red lines indicate the position of atomic columns in the absence of screw dislocation. The orange arrows point to atomic columns around the screw dislocation core. The sample was grown with $G = 2 \frac{\text{°C}}{\text{cm}}$ and $v = 3.3 \frac{\text{mm}}{\text{s}}$ (Figure S2, Supporting Information).

“Eshelby twist”^[39] (strain-induced rotation of the crystal lattice around an axial screw).

As the system cools to below the metastable eutectic temperature, the Zn phase forms heteroepitaxially along the spiral growth steps of MgZn_2 (Figure 5C). That is, the Zn phase forms exclusively along the ledges and not on the $\{0001\}_{\text{MgZn}_2}$ terraces, assuming that the supersaturation of Zn is not too high. Only at supersaturations above the threshold of forming 2D nuclei (the kinetic roughening transition^[40]) will island growth be possible on the basal plane. Once Zn has nucleated along the spiral steps, it grows in a coupled manner with the MgZn_2 phase. The interphase spacing (Figures S2 and S5, Supporting Information) is set by the undercooling for lamellar growth according to the Jackson–Hunt model.^[28] During the ensuing eutectic growth, low-energy solid–solid interfaces $\{70\bar{7}2\}_{\text{MgZn}_2}$ are maintained. As demonstrated in Note S4, Supporting Information, these interfaces have an approximately eightfold lower energy compared to those solid–solid interfaces in the irregular Zn– MgZn_2 eutectic. Phase field simulations^[41] show that in these so-called “locked” eutectic grains, the interphase boundaries follow specific crystallographic growth direction such that the lamellae can be tilted relative to an imposed thermal gradient. Ultimately, the conical faceted enveloping shape of the eutectic colony is determined by the anisotropy of the interphase boundary energy, and not the Wulff shape of MgZn_2 (a hexagonal rod). Within each colony, spiraling sheets of the fully faceted MgZn_2 phase are arranged with near-constant periodicity. This regular organization of lamellae is somewhat anomalous for an irregular eutectic (the Jackson α -factor for the MgZn_2 phase is at most 5.7). Given that the eutectic spirals nucleate atop axial screw dislocations, the regularity of the two phases is enforced by the spiral growth steps themselves. The fully developed spiral colony (Figure 5D) illustrates the solid–solid interfaces, intra-facet angle, and growth direction.

The nucleation behavior of the spiral Zn– MgZn_2 eutectic represents a surprising inversion of our conventional wisdom. It has long been thought^[42] that complex regular structures

arise due to morphological instabilities at the eutectic growth front, such that the solid–liquid interface is comprised of an array of macro-faceted cellular projections that enable a regular structure to develop (orthogonal to the macro-facet). This is the case for the complex regular, rod-like Zn– $\text{Mg}_2\text{Zn}_{11}$ eutectic, wherein parallel, regularly spaced lamellae connect to a common trigonal spine. Yet this classical viewpoint cannot explain the complex regular spiral morphology of Zn– MgZn_2 . Instead, crystallographic defects (screw dislocations) of the primary MgZn_2 Laves phase catalyze the heterogeneous nucleation of the eutectic phases during solidification. That is, the presence of such crystallographic defects causes the spiral growth form. While screw dislocation-driven growth has been reported in diverse areas of crystallization^[37,43–46]—and indeed extensions of the Burton–Cabrera–Frank^[30] spiral growth model exist^[47]—our proposed mechanism on the role of “hidden” polytetrahedral phases in assisting heterogeneous nucleation supports and expands upon recent reports,^[11,48] for instance, metastable quasicrystal-induced nucleation yielding grain-refined alloys,^[49] among other two-step solidification pathways.

3. Conclusions

We have synthesized spiral, two-phase microstructures that possess an intrinsic chirality and a faceted, periodic architecture. Correlative characterization facilitated by data science methods reveals the formation mechanism as well as the morphological and heteroepitaxial relationships between the phases that grant the microstructure its unique spiral pattern. We find the macroscopic spirals emerge via microscopic defects through a two-step crystallization process. First, polytetrahedral phases nucleate readily in the liquid owing to their low interfacial energy. These nucleation precursors provide favorable environments (screw dislocations) for crystallization of the spiral eutectic, thereby demonstrating the broad applicability of Frank’s defect-driven growth mechanism

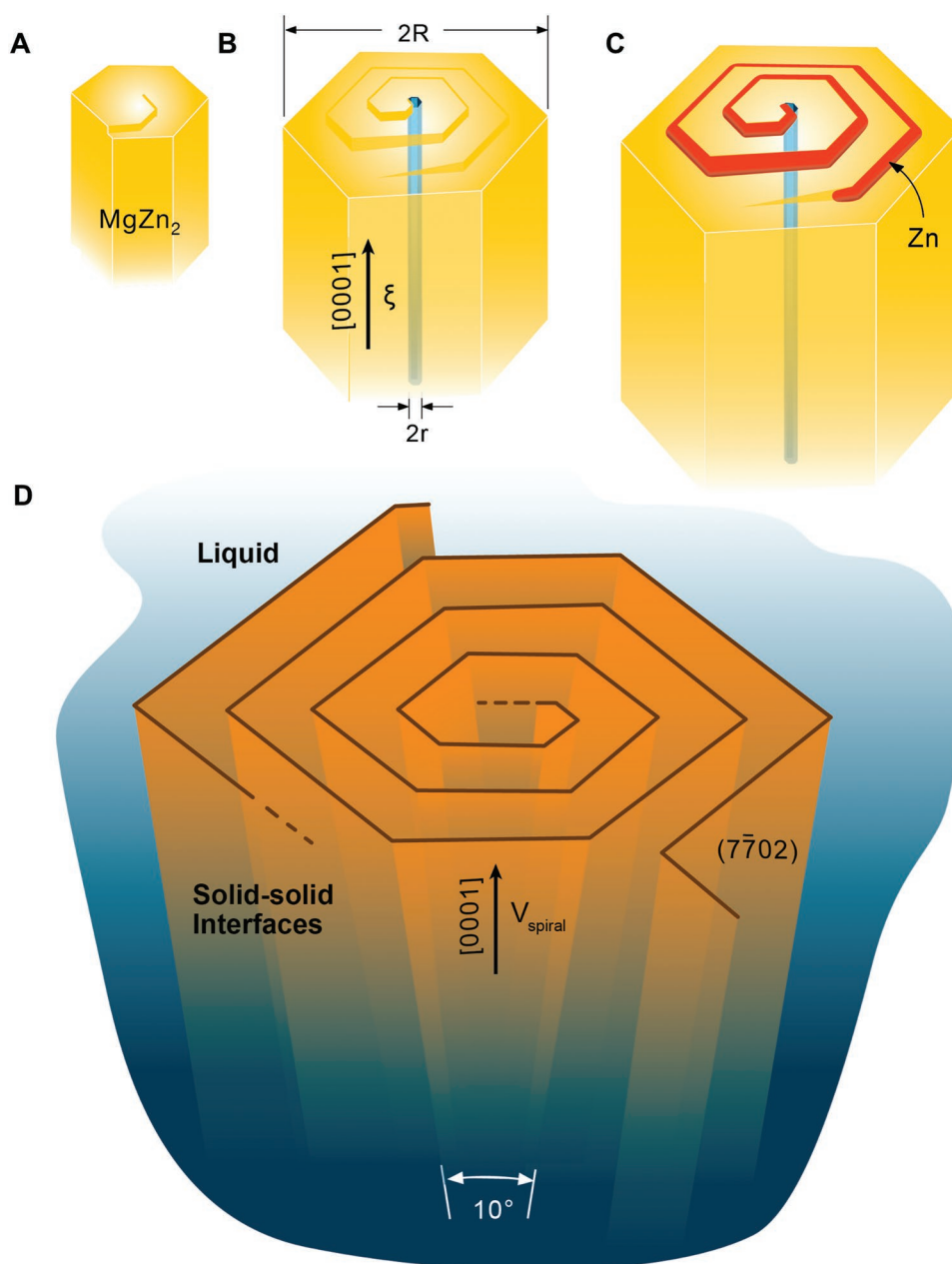


Figure 5. Illustration of the screw dislocation mediated growth of spiral eutectics. A) Establishment of a spiral ramp due to axial screw dislocation on the seed MgZn_2 crystal. The ramp provides self-perpetuating steps that enable spiral growth. B) Growth of the seed crystal and formation of a hollow core. The axial growth direction of the spiral is along $[0001]_{\text{MgZn}_2}$. For sufficiently large Burgers vector, the strain energy is alleviated by hollowing out the dislocation core (thin blue cylinder), in agreement with Frank's hollow-tube mechanism.^[30] Radii of the seed and hollow-core are R and r , respectively; ξ is the sense vector of the dislocation. C) Heteroepitaxial growth of Zn (red, not to scale) along the exposed MgZn_2 growth steps (ledges). D) Spiral eutectic colony during the growth process. Only solid–solid interfaces are shown for clarity. The habit planes of the spiral are $\{7\bar{7}02\}_{\text{MgZn}_2}$. The intra-facet angle is $\approx 10^\circ$, for example, between $\{7\bar{7}02\}$ and $\{70\bar{7}2\}$.

to multi-phase materials. Our 3D studies provide the necessary benchmark data for simulations of complex self-organization patterns, thus expanding the horizon for the design of next-generation alloys with superior properties. Spiral self-organization may open exciting opportunities in photonics, where the resulting multi-phase structures can serve as templates for rapid fabrication or additive manufacturing of 3D chiral photonic crystals.

4. Experimental Section

Synthesis of Eutectic Microstructures by Directional Solidification: Alloy buttons of nominal composition Zn-3 wt% Mg were cast via vacuum arc-remelting at the Materials Preparation Center at Ames Laboratory (Ames, IA, USA), using 99.999% purity Zn and 99.99% purity Mg. The as-prepared alloy buttons were cut in the shape of cylindrical rods of 1 mm diameter by 5 mm length via electrical discharge machining. In such small samples, convection effects have been shown to be

negligible.^[50] Two-phase eutectics were then grown by directional solidification using a three-zone vertical Bridgman furnace (MTI Corporation EQ-SKJ-BG). The temperature gradient was imposed onto the fully molten sample by independently fixing the temperatures of the three zones. The growth velocity was controlled by the upward, simultaneous movement of the zones (sample stationary). Some samples were also prepared by “gradient freeze,” wherein both the sample and the heating zones remained stationary while the zone temperatures were decreased at fixed rates under the imposed thermal gradient (we note that the cooling rate is the product of the thermal gradient and growth velocity).

Laser Micromachining for Nano-Tomography Experiments: The directionally solidified samples were polished to a mirror finish and imaged on an optical microscope (ZEISS Axio Imager 2, Carl Zeiss Microscopy Inc., Oberkochen, Germany) to locate the spiral regions of interest. Local features were identified as fiducials for further sample preparation. The specimens were then transferred to a picosecond laser ablation based micro-machining system (microPREP, 3D-Micromac AG, Chemnitz, Germany). The region-of-interest was registered using the built-in light microscope, and cylindrical micropillars 60 μm in diameter were milled top-down measuring nominally 100 μm in height. The pillars were extracted and mounted on tungsten needles for imaging in X-ray nano-tomography.

X-Ray Nano-Tomography: Non-destructive 3D imaging was performed on a ZEISS Xradia Ultra 800 (Carl Zeiss X-ray Microscopy Inc, Pleasanton CA), a nanoscale X-ray microscope with an 8.0 keV copper source. The tomography acquisition consisted of 901 X-ray projection images collected at a 130 s exposure/frame with a 64 nm/voxel resolution in the large field-of-view mode. The 3D reconstructed slices were produced by processing the projection images in the accompanying Reconstructor software, which is based on a parallel-beam filtered back projection algorithm. Output files consisted of a stack of 16-bit 3D dataset with 1024 × 1024 × 1024 pixel dimensions. The reconstructed data was rendered and analyzed using a 3D visualization software (Dragonfly 3.6, Object Research Systems [ORS] Inc, Montreal, Canada, 2018). Additionally, two-class segmentation of reconstructed datasets was performed using an interactive pixel classifier segmentation tool based on a random forest classifier within Ilastik 1.2 (Ilastik: Interactive Learning and Segmentation Toolkit).^[51]

Electron Backscatter Diffraction: The 3D EBSD measurements were performed on a ZEISS Crossbeam 550 L focused-ion beam-scanning electron microscope (FIB-SEM) equipped with an Oxford Instrument Symmetry EBSD camera and an Oxford Instrument ULTIM MAX 170 electron dispersive spectroscopy (EDS) detector. The data were acquired using the ZEISS Atlas 5 3D software for FIB-SEM tomography. Standard Atlas 5 3D preparation with protective deposition and tracking fiducials was carried out. To avoid damage to beam-sensitive phases, an energy of 15 kV was chosen for the FIB milling with a probe current of 4 nA. SEM images were acquired using 2 kV SEM beam energy and 2 nA of beam current. Chamber secondary electrons (SE) and Inlens SE detectors were used in parallel. An isotropic voxel resolution of 10 nm was chosen for the imaging, that is, 10 nm pixel resolution within the images and 10 nm slice thickness for the FIB milling. Atlas 5 was used to measure and track the actual slice thickness and adapt the milling progress accordingly, also compensating for sample drift. A voxel resolution of 70 or 100 nm was chosen for the EBSD measurements. Thus, every 7th or 10th image, the sample was automatically moved to EBSD position, and the map acquisition was started. SEM conditions were changed automatically to 19 kV beam energy and 20 nA of beam current, to assure high signal-to-noise EBSD patterns. EDS maps were acquired in parallel. Pixel resolution of the analytic maps was set to 70 or 100 nm, respectively, to achieve isotropic voxels. The Symmetry EBSD camera was set to binning mode “Speed 2” with an exposure time of 1 ms EBSD slices were registered in DREAM.3D software (BlueQuartz) using a misorientation tolerance of 5°. The registered data were subsequently rendered in 3D through the open-source visualization software ParaView (Kitware).^[52] Crystallographic analysis of the individual EBSD slices (texture data) was performed using the MATLAB (The MathWorks, Inc.) toolbox MTEX.^[53]

In Situ Synchrotron High-Energy X-Ray Diffraction: The HEXRD experiments were conducted at Sector 11-ID-C of the Advanced Photon Source in Argonne National Laboratory (Argonne, IL, USA). The solidification experiments were performed in sealed quartz tubes under the protection of a high-purity argon atmosphere. The sample was heated, melted, and overheated using a radio frequency induction-heating coil with a maximum heating power of 4.2 kW. Then, the power of the heating coil was switched off. The molten sample was cooled and solidified spontaneously. The cooling rate was assumed to be constant (around 20 K s⁻¹) since cooling is dominated by thermal radiation from the sample surface. The sample was melted and solidified eight times. In each cycle of melting and solidification, a monochromatic X-ray source with wavelength of 0.1173 Å was incident on the sample through a large gap between two wings of the induction coil. The diffracted X-rays were scattered in forward directions and were recorded continuously with an exposure time of 0.5 s using a Perkin-Elmer amorphous silicon detector at a distance of about 1.8 m from the sample. The maximum active area of the detector is 409.6 mm × 409.6 mm, with 2048 × 2048 pixels and a pixel size of 0.2 mm × 0.2 mm. After the experiments, the sample-to-detector distance was calibrated using a standard sample of CeO₂ at room temperature. The recorded 2D diffraction patterns were integrated using the FIT2D software^[54] (v.12.077) for phase identification. Background subtraction was performed using the High-Score software (Malvern Panalytical). Combining Bragg's law and lattice spacing of crystal structure allowed for determination of phase formation sequence.

Electron Microscopy: All specimens for S/TEM were prepared via focused-ion beam (FIB) lift-out technique in an FEI Helios 650 Nanolab SEM/FIB. Lift-out samples were thinned to ≈80 nm and cleaned equally on both sides. The damage from Ga beam was limited to the top 100–120 nm of the final sample, which was avoided in all subsequent S/TEM experiments. Samples were plasma cleaned for 5 min prior to insertion into the S/TEM. The diffraction-contrast TEM experiments were performed with a JEOL 2010F microscope operating at 200 kV. All STEM experiments used a JEOL 3100R05 double-Cs corrected S/TEM with an operating voltage of 300 kV. All cross-sectional SEM and compositional maps were collected on a TESCAN MIRA3 SEM on mirror-finish polished samples; the micrographs were collected using both secondary and backscattered electrons with an operating voltage of 10–20 kV.

Supporting Information

Supporting Information is available from the Wiley Online Library or from the author.

Acknowledgements

The authors gratefully acknowledge the financial support from the Air Force Office of Scientific Research Young Investigator Program under award no. FA9550-18-1-0044. The authors express their thanks to Profs. Julia Dshemuchadse, Sharon Glotzer, John Heron, and Amit Misra for a critical reading of the manuscript. The authors acknowledge the financial support of the University of Michigan College of Engineering and NSF grants DMR-9871177 and DMR-0723032, which support the Michigan Center for Materials Characterization at the University of Michigan. The authors also thank the technical support of this Center. Y.W. thanks the China Scholarship Council for a visiting Ph.D. fellowship. This research used resources of the Advanced Photon Source, U.S. Department of Energy (DOE) Office of Science User Facility operated for the DOE Office of Science by Argonne National Laboratory under contract no. DE-AC02-06CH11357.

Conflict of Interest

The authors declare no conflict of interest.

Keywords

chirality, crystallization, self-organization, spiral eutectics

Received: October 25, 2019

Revised: December 27, 2019

Published online:

- [1] J. J. De Yoreo, P. U. P. A. Gilbert, N. A. J. M. Sommerdijk, R. L. Penn, S. Whitelam, D. Joester, H. Zhang, J. D. Rimer, A. Navrotsky, J. F. Banfield, A. F. Wallace, F. M. Michel, F. C. Meldrum, H. Cölfen, P. M. Dove, *Science* **2015**, *349*, aaa6760.
- [2] J. Baumgartner, A. Dey, P. H. H. Bomans, C. Le Coadou, P. Fratzl, N. A. J. M. Sommerdijk, D. Faivre, *Nat. Mater.* **2013**, *12*, 310.
- [3] W. J. E. Habraken, J. Tao, L. J. Brylka, H. Friedrich, L. Bertineti, A. S. Schenk, A. Verch, V. Dmitrovic, P. H. H. Bomans, P. M. Frederik, J. Laven, P. Van Der Schoot, B. Aichmayer, G. De With, J. J. DeYoreo, N. A. J. M. Sommerdijk, *Nat. Commun.* **2013**, *4*, 1507.
- [4] R. L. Penn, J. F. Banfield, *Science* **1998**, *281*, 969.
- [5] N. D. Loh, S. Sen, M. Bosman, S. F. Tan, J. Zhong, C. A. Nijhuis, P. Král, P. Matsudaira, U. Mirsaidov, *Nat. Chem.* **2017**, *9*, 77.
- [6] M. C. Weidman, D. M. Smilgies, W. A. Tisdale, *Nat. Mater.* **2016**, *15*, 775.
- [7] Z. R. Tian, J. A. Voigt, J. Liu, B. Mckenzie, M. J. Mcdermott, M. A. Rodriguez, H. Konishi, H. Xu, *Nat. Mater.* **2003**, *2*, 821.
- [8] J. F. Lutsko, *Sci. Adv.* **2019**, *5*, eaav7399.
- [9] V. Uzunova, W. Pan, V. Lubchenko, P. G. Vekilov, *Faraday Discuss.* **2012**, *159*, 87.
- [10] V. A. Stoica, N. Laanait, C. Dai, Z. Hong, Y. Yuan, Z. Zhang, S. Lei, M. R. McCarter, A. Yadav, A. R. Damodaran, S. Das, G. A. Stone, J. Karapetrova, D. A. Walko, X. Zhang, L. W. Martin, R. Ramesh, L. Q. Chen, H. Wen, V. Gopalan, J. W. Freeland, *Nat. Mater.* **2019**, *18*, 377.
- [11] G. Kurtuldu, K. F. Shamlaye, J. F. Löffler, *Proc. Natl. Acad. Sci. U. S. A.* **2018**, *115*, 6123.
- [12] T. Yang, Y. L. Zhao, Y. Tong, Z. B. Jiao, J. Wei, J. X. Cai, X. D. Han, D. Chen, A. Hu, J. J. Kai, K. Lu, Y. Liu, C. T. Liu, *Science* **2018**, *362*, 933.
- [13] J. S. Bangsund, T. R. Fielitz, T. J. Steiner, K. Shi, J. R. Van Sambeek, C. P. Clark, R. J. Holmes, *Nat. Mater.* **2019**, *18*, 725.
- [14] A. A. Kulkarni, J. Kohanek, K. I. Tyler, E. Hanson, D. U. Kim, K. Thornton, P. V. Braun, *Adv. Opt. Mater.* **2018**, *6*, 1800071.
- [15] I. Jozwik-Biala, A. Klos, J. Toudert, H. B. Surma, M. Gajc, P. Dluzewski, K. Sobczak, K. Sadecka, K. Orlinski, D. A. Pawlak, *Adv. Opt. Mater.* **2014**, *3*, 381.
- [16] C. M. Soukoulis, M. Wegener, *Nat. Photonics* **2011**, *5*, 523.
- [17] G. A. Chadwick, *Prog. Mater. Sci.* **1963**, *12*, 99.
- [18] P. Steinmetz, S. Gadkari, A. Genau, *J. Cryst. Growth* **2019**, *507*, 425.
- [19] R. L. Fullman, D. L. Wood, *Acta Metall.* **1954**, *2*, 188.
- [20] J. D. Hunt, P. Chilton, *J. Inst. Met.* **1966**, *93*, 146.
- [21] A. Dippenaar, H. D. W. Bridgman, G. A. Chadwick, *J. Inst. Met.* **1971**, *99*, 137.
- [22] H. Y. Liu, H. Jones, *Acta Metall. Mater.* **1992**, *40*, 229.
- [23] D. D. Double, P. Truelove, A. Hellawell, *J. Cryst. Growth* **1968**, *2*, 191.
- [24] S. Akamatsu, M. Perrut, S. Bottin-Rousseau, G. Faivre, *Phys. Rev. Lett.* **2010**, *104*, 056101.
- [25] G. Tegze, G. I. Tóth, *Acta Mater.* **2012**, *60*, 1689.
- [26] J. Hötzer, P. Steinmetz, M. Jainta, S. Schulz, M. Kellner, B. Nestler, A. Genau, A. Dennstedt, M. Bauer, H. Köstler, U. Rude, *Acta Mater.* **2016**, *106*, 249.
- [27] T. Pusztai, L. Rátkai, A. Szállás, L. Gránásy, *Phys. Rev. E* **2013**, *87*, 032401.
- [28] K. Jackson, J. Hunt, *Trans. Metall. Soc. AIME* **1966**, *236*, 1129.
- [29] L. E. O. Breiman, *Mach. Learn.* **2001**, *45*, 5.
- [30] W. K. Burton, N. Cabrera, F. C. Frank, *Nature* **1949**, *163*, 398.
- [31] J. W. Edington, in *Interpretation of Transmission Electron Micrographs*, Macmillan Education, London **1975**, pp. 1–112.
- [32] A. Jain, S. P. Ong, G. Hautier, W. Chen, W. D. Richards, S. Dacek, S. Cholia, D. Gunter, D. Skinner, G. Ceder, K. A. Persson, *APL Mater.* **2013**, *1*, 011002.
- [33] J. Russo, H. Tanaka, *Sci. Rep.* **2012**, *2*, 505.
- [34] F. Spaepen, *Nature* **2000**, *408*, 781.
- [35] D. Holland-Moritz, D. M. Herlach, K. Urban, *Phys. Rev. Lett.* **1993**, *71*, 1196.
- [36] H. Reichert, O. Klein, H. Dosch, M. Denk, V. Honkimäki, T. Lippmann, G. Reiter, *Nature* **2000**, *408*, 839.
- [37] S. A. Morin, M. J. Bierman, J. Tong, S. Jin, *Science* **2010**, *328*, 476.
- [38] B. Sung, A. De La Cotte, E. Grelet, *Nat. Commun.* **2018**, *9*, 1405.
- [39] J. D. Eshelby, *J. Appl. Phys.* **1953**, *24*, 176.
- [40] D. E. Temkin, *Crystallization Processes*, Consultants Bureau, New York **1966**.
- [41] S. Ghosh, A. Choudhury, M. Plapp, S. Bottin-Rousseau, G. Faivre, S. Akamatsu, *Phys. Rev. E* **2015**, *91*, 22407.
- [42] R. Elliott, in *Eutectic Solidification Processing*, Butterworth-Heinemann, Oxford **2013**, pp. 120–156.
- [43] Z. Zhu, D. S. Goldfarb, M. D. Ward, J. D. Rimer, J. A. Wesson, Z. An, M. H. Lee, *Science* **2010**, *330*, 337.
- [44] M. J. Bierman, Y. K. A. Lau, A. V. Kvit, A. L. Schmitt, S. Jin, *Science* **2008**, *320*, 1060.
- [45] F. Ding, A. R. Harutyunyan, B. I. Yakobson, *Proc. Natl. Acad. Sci. U. S. A.* **2009**, *106*, 2506.
- [46] Y. Liu, J. Wang, S. Kim, H. Sun, F. Yang, Z. Fang, N. Tamura, R. Zhang, X. Song, J. Wen, B. Z. Xu, M. Wang, S. Lin, Q. Yu, K. B. Tom, Y. Deng, J. Turner, E. Chan, D. Jin, R. O. Ritchie, A. M. Minor, D. C. Chrzan, M. C. Scott, J. Yao, *Nature* **2019**, *570*, 358.
- [47] R. C. Snyder, M. F. Doherty, *Proc. R. Soc. A* **2009**, *465*, 1145.
- [48] W. Hornfeck, R. Kobold, M. Kolbe, M. Conrad, D. Herlach, *Nat. Commun.* **2018**, *9*, 4054.
- [49] G. Kurtuldu, A. Sicco, M. Rappaz, *Acta Mater.* **2014**, *70*, 240.
- [50] J. H. Lee, S. Liu, R. Trivedi, *Metall. Mater. Trans. A* **2005**, *36*, 3111.
- [51] C. Sommer, C. Straehle, U. Kothe, F. A. Hamprecht, in *IEEE Int. Symp. Biomed. Imaging*, IEEE, Piscataway, NJ **2011**, pp. 230–233.
- [52] J. Ahrens, B. Geveci, C. Law, in *The Visualization Handbook*, Elsevier, New York **2005**, pp. 717–731.
- [53] F. Bachmann, R. Hielscher, H. Schaeben, *Solid State Phenom.* **2010**, *160*, 63.
- [54] A. Hammersley, The FIT2D Home Page, <http://www.esrf.eu/computing/scientific/FIT2D/> (accessed: September 2019).